Title:

Creep deformation and rafting in nickel-based superalloys simulated by phase-field method using classical flow and creep theories

Author names:

Yuhki TSUKADA[a,*], Yoshinori MURATA[a], Toshiyuki KOYAMA[b], Nobuhiro MIURA[c], and Yoshihiro KONDO[c]

Affiliations:

[a] Department of Materials, Physics and Energy Engineering, Graduate School of Engineering, Nagoya University, Furo-cho, Chikusa-ku, Nagoya 464-8603, Japan

[b] Department of Materials Science and Engineering, Graduate School of Engineering, Nagoya Institute of Technology, Gokiso-cho, Showa-ku, Nagoya 466-8555, Japan

[c] Department of Mechanical Systems Engineering, School of Systems Engineering, National Defense Academy, 1-10-20 Hashirimizu, Yokosuka 239-8686, Japan

[*]Corresponding author:

Tel.: +81-52-789-5342

Fax: +81-52-789-3232

E-mail address: tsukada@silky.numse.nagoya-u.ac.jp

Abstract

A phase-field model has been developed to simulate the evolution of both ($\gamma + \gamma'$) microstructure and inelastic strain between γ' phases (i.e., γ channel) during high-temperature creep in nickel-based superalloys. Inelastic strain is defined as the sum of time-independent and time-dependent components. Previously reported mechanical properties of single-phase γ alloys are considered in the calculation of inelastic strain evolution. A two-dimensional phase-field simulation is performed, and the results of microstructure evolution and creep rate versus time curve are fitted to the experimental data of the high-temperature creep of CMSX-4. The slope of the creep rate versus time curve in the initial stage of transient creep, plasticity preference in different types of γ channels, and rafting phenomenon are reproduced well by the simulation. Furthermore, it is demonstrated that the creep rate increases locally at γ/γ' interfaces when the rafted structure is formed.

Keywords: Phase-field method; Nickel-based superalloys; Plasticity; Creep; Directional coarsening

1. Introduction

Nickel-based single-crystal superalloys exhibit superior creep strength at high temperatures and are used as gas turbine materials. The excellent mechanical properties of these alloys are attributed to the γ' strengthening phase ($L1_2$ structure) that precipitates coherently in the γ phase having a face-centered cubic lattice. During heat treatment for precipitation without external stress, the cuboidal γ' phase is arranged along <100> crystallographic directions in the γ matrix. On the other hand, directional coarsening of the γ' phase occurs in high-temperature creep under [001] tensile stress; the γ' phase coarsens in a direction normal to the external stress axis, resulting in the formation of the so-called rafted structure [1], in which the γ' phase becomes lamellar. The rafted structure collapses under long-term creep at high temperatures. It has been reported that the lamellar thickness of the rafted structure increases [2], or the lamellar structure develops a wavelike shape [3−5]. The creep rupture life of superalloys strongly depends on such morphological stability of the (γ + γ') two-phase microstructure. Miura et al. confirmed that the creep rate in the accelerating creep stage of CMSX-4 is correlated with increase in the γ-channel width [2]. Hence, quantitative prediction of microstructure evolution during creep is one important subject in material development of superalloys.

The initial stage of creep deformation, arising from plastic deformation of the γ channels, strongly affects the rafting phenomenon. It has been demonstrated by a finite element analysis that the rafting phenomenon needs to be treated in the elasto-plastic regime and that creep flow in the γ matrix should be considered [6]. Simulation studies using the phase-field method also indicate that the γ-channel plasticity results in a large driving force for rafting [7−10], and affects the morphological stability of the rafted structure [11,12]. These phase-field simulations simultaneously model both (γ + γ') coherent microstructure evolution and plastic deformation in the γ phase. In addition, some phase-field simulations

have revealed the role of elastic inhomogeneity (the elastic modulus mismatch between the precipitate and matrix phases) in microstructure evolution [8,9,12−14]. This inhomogeneity affects particle-size distribution, coarsening rate of the γ' phase in precipitation aging [12,14], and rafting kinetics during creep [8,9]. Although these parametric studies, using the phase-field method, have led to fundamental understanding of the effect of material parameters on morphological evolution, a quantitative simulation of microstructure evolution correlated with creep strength is still desired.

For the quantitative simulation, high-temperature creep properties of Ni−20 mass% Cr single crystals, a model alloy for the γ matrix of nickel-based superalloys, are available [15−17]. This alloy shows (i) negligible decrease in creep rate during the transient stage and (ii) a five-power-law relationship at a strain of 0.01 under low stresses [16,17]. On the other hand, in an elasto-plastic phase-field model [18−20], the evolution of plastic strain fields is described by an equation similar to that of classical flow theory. This model can incorporate experimental mechanical properties in the phase-field method, and serve as a basis for the quantitative simulation of rafting phenomenon during high-temperature creep.

The aim of this study is to develop a model that simultaneously treats the evolution of both (γ + γ') microstructure and inelastic strain in the γ phase. Inelastic strain in the γ matrix is defined as the sum of time-independent and time-dependent components. The evolution of each strain is described on the basis of the classical flow and creep theories that incorporate the previously reported mechanical properties of γ-phase alloys. The results of this simulation are fitted to the experimental data of high-temperature creep of CMSX-4 as a practical alloy. The validity of the developed model is also discussed. In particular, we focus on reproducibility of a creep rate versus time curve and the corresponding microstructure evolution of the practical alloy.

2. Calculation method

4

2.1. Phase-field model

To describe the (γ + γ') two-phase microstructure, the γ' volume fraction field $f(\mathbf{r},t)$, and four artificial order parameter fields $\phi_i(\mathbf{r},t)$, (i = 1, 2, 3, 4), are employed. $\phi_i(\mathbf{r},t)$ describes the four ordered domains in the γ' phase, and is equal to 0 within the γ phase and 1 within the ith γ' domain [21]. These field variables change spatially (**r**) and temporally (t), and are continuous across the γ/γ' interfacial regions. In general, the composition field ($c(\mathbf{r},t)$) is used as a field variable. In this study, the γ' volume fraction field is assumed to be related to the composition field as

$$f(\mathbf{r},t) = \frac{c(\mathbf{r},t) - c_{\mathrm{m}}^0}{c_{\mathrm{p}}^0 - c_{\mathrm{m}}^0},$$

(1)

where c_{m}^0 and c_{p}^0 are the equilibrium compositions of the γ and γ' phases, respectively. Hence, $f(\mathbf{r},t)$ is treated as a conserved field variable in the subsequent description. The temporal evolution of the field variables is given by the following Cahn−Hilliard and Allen−Cahn equations [22]:

$$\frac{\partial f(\mathbf{r},t)}{\partial t} = M\nabla^2 \frac{\delta G}{\delta f(\mathbf{r},t)},$$

(2)

$$\frac{\partial \phi_i(\mathbf{r},t)}{\partial t} = -L\frac{\delta G}{\delta \phi_i(\mathbf{r},t)}, \ (i = 1, 2, 3, 4),$$

(3)

where G is the total free energy of the microstructure, M is the diffusion mobility, and L is the structural relaxation coefficient. The total free energy is given by

$$G = \int_{\mathbf{r}} \left[\begin{array}{c} \{1 - h(\phi_i)\} G_{\text{chem}}^{\text{m}}(f^{\text{m}}) + h(\phi_i) G_{\text{chem}}^{\text{p}}(f^{\text{p}}) + w g(\phi_i) \\ + \dfrac{\kappa_\phi}{2} \displaystyle\sum_{i=1}^{4} (\nabla \phi_i)^2 + E_{\text{str}} \end{array} \right] d\mathbf{r} , \tag{4}$$

where $G_{\text{chem}}^{\text{m}}$ and $G_{\text{chem}}^{\text{p}}$ are the chemical free-energy densities of the γ and γ' phases, respectively, $h(\phi_i)$ is a continuous function having values between 0 and 1, $g(\phi_i)$ is the double-well potential, w is the double-well potential height [21,23], κ_ϕ is the gradient energy coefficient [24], and E_{str} is the elastic strain energy density.

The Gibbs free energy of each phase is calculated as a function of both composition and temperature by using the thermodynamic database of the equilibrium phase diagram. In this study, free-energy densities are approximated as quadratic functions of the γ' volume fraction field:

$$G_{\text{chem}}^{\text{m}} = \frac{1}{2} W_{\text{m}} f^2 , \tag{5}$$

$$G_{\text{chem}}^{\text{p}} = \frac{1}{2} W_{\text{p}} (1 - f)^2 , \tag{6}$$

where W_{m} and W_{p} are coefficients determined by fitting the calculated Gibbs energy curves of both phases. The functions $h(\phi_i)$ and $g(\phi_i)$ in Eq. (4) are selected as [21]

$$h(\phi_i) = \sum_{i=1}^{4} [\phi_i^3 (10 - 15 \phi_i + 6 \phi_i^2)] , \tag{7}$$

$$g(\phi_i) = \sum_{i=1}^{4} [\phi_i^2 (1 - \phi_i)^2] + \alpha \sum_{i=1}^{4} \sum_{j \neq i}^{4} \phi_i^2 \phi_j^2 . \tag{8}$$

6

By using the description proposed by Kim et al. [25], the interface region is regarded as a mixture of the γ and γ' phases having different γ' volume fractions, f^{m} and f^{p}, but equal chemical potentials:

$$f = \{1 - h(\phi_i)\} f^{\mathrm{m}} + h(\phi_i) f^{\mathrm{p}}, \tag{9}$$

$$\left(\frac{\partial G_{\mathrm{chem}}^{\mathrm{m}}}{\partial f} \right)_{f = f^{\mathrm{m}}} = \left(\frac{\partial G_{\mathrm{chem}}^{\mathrm{p}}}{\partial f} \right)_{f = f^{\mathrm{p}}}. \tag{10}$$

From Eqs. (9) and (10), we obtain a single solution pair of f^{m} and f^{p}.

According to the diffuse-interface description, excess free energy exists at interfaces because of the inhomogeneity of field variables, and the excess energy is related to the interfacial energy between the γ/γ' interfaces [22]. The parameters w and κ_ϕ in Eq. (4) are determined using $\gamma_{\mathrm{s}} = \sqrt{w \kappa_\phi} / 3\sqrt{2}$ and $2\lambda = \alpha \sqrt{2\kappa_\phi / w}$, where γ_{s} is the interfacial energy per area and 2λ is the interfacial thickness. α is a coefficient that depends on the definition of interfacial thickness and is set to $\alpha = 2$ [24].

The elastic strain energy density is calculated by the general equation [26,27]:

$$E_{\mathrm{str}} = \frac{1}{2} C_{ijkl}(\mathbf{r}) \varepsilon_{ij}^{\mathrm{el}}(\mathbf{r}) \varepsilon_{kl}^{\mathrm{el}}(\mathbf{r}) - \sigma_{ij}^{\mathrm{appl}} \bar{\varepsilon}_{ij}, \tag{11}$$

where C_{ijkl} is the elastic constant, $\varepsilon_{ij}^{\mathrm{el}}$ is the elastic strain, and $\sigma_{ij}^{\mathrm{appl}}$ is the applied stress. The elastic strain is expressed as

$$\varepsilon_{kl}^{\mathrm{el}}(\mathbf{r}) = \varepsilon_{kl}(\mathbf{r}) - \varepsilon_{kl}^{0}(\mathbf{r}), \tag{12}$$

where ε_{kl} is the total strain and ε_{kl}^{0} is the eigenstrain. This eigenstrain is defined as the sum of three terms:

$$\varepsilon_{kl}^{0}(\mathbf{r}) = \varepsilon_{0}\delta_{kl}h(\phi_{i}) + \varepsilon_{kl}^{p}(\mathbf{r}) + \varepsilon_{kl}^{c}(\mathbf{r}) \,, \tag{13}$$

where δ_{kl} is the Kronecker delta function, ε_{kl}^{p} is the plastic strain, and ε_{kl}^{c} is the creep strain. The first term in Eq. (13) is the lattice misfit strain between the γ and γ' phases, and is defined as a linear function of $h(\phi_{i})$. ε_{0} is the lattice misfit given by $\varepsilon_{0} = (a_{p} - a_{m})/a_{m}$, where a_{m} and a_{p} are the lattice parameters of the γ and γ' phases, respectively. ε_{kl}^{p} and ε_{kl}^{c} cannot be strictly separated from each other. As mentioned in Sections 2.2 and 2.3, ε_{kl}^{p} is defined as "time-independent inelastic strain" while ε_{kl}^{c} is defined as "time-dependent inelastic strain." The total strain ε_{kl} in Eq. (12) is represented as the sum of the homogeneous strain ($\bar{\varepsilon}_{kl}$) and the heterogeneous strain ($\delta\varepsilon_{kl}$):

$$\varepsilon_{kl}(\mathbf{r}) = \bar{\varepsilon}_{kl} + \delta\varepsilon_{kl}(\mathbf{r}) \,. \tag{14}$$

The homogeneous strain is given by $\bar{\varepsilon}_{kl} = 1/V \int_{\mathbf{r}} \varepsilon_{kl}^{0}(\mathbf{r})d\mathbf{r} + \varepsilon_{kl}^{appl}$ under a stress-controlled boundary condition, where V is the system volume. The heterogeneous strain is expressed as

$$\delta\varepsilon_{kl}(\mathbf{r}) = \frac{1}{2}\left\{ \frac{\partial u_{k}(\mathbf{r})}{\partial r_{l}} + \frac{\partial u_{l}(\mathbf{r})}{\partial r_{k}} \right\} \,, \tag{15}$$

where u_{k} represents the kth component of the elastic displacement. Hooke's law gives the local elastic stress as $\sigma_{ij}^{el}(\mathbf{r}) = C_{ijkl}(\mathbf{r})\varepsilon_{kl}^{el}(\mathbf{r})$. By considering elastic inhomogeneity, the local elastic constant is assumed to be $C_{ijkl}(\mathbf{r}) = \{1 - h(\phi_{i})\}C_{ijkl}^{m} + h(\phi_{i})C_{ijkl}^{p}$, where C_{ijkl}^{m} and C_{ijkl}^{p}

represent the elastic constants of the γ and γ' phases, respectively. Using the local equilibrium equation ($\partial \sigma_{ij}^{\mathrm{el}} / \partial r_j = 0$), we calculate the local displacement field ($\mathbf{u}$) in Fourier space. Because inhomogeneity is introduced in the elastic constant, an iterative approach is adopted for solving the inhomogeneous elasticity equation [28].

2.2. Evolution of plastic strain

The plastic strain $\varepsilon_{kl}^{\mathrm{p}}$ in Eq. (13) is defined as time-independent plasticity that is primarily introduced in a material as a part of instantaneous strain in a creep test. The evolution of plastic strain is described by the following equation [18−20]:

$$\frac{\partial \varepsilon_{ij}^{\mathrm{p}}(\mathbf{r}_{\mathrm{p}}, \tau)}{\partial \tau} = -K_{ijkl} \frac{\delta E_{\mathrm{shear}}}{\delta \varepsilon_{kl}^{\mathrm{p}}(\mathbf{r}_{\mathrm{p}}, \tau)}, \tag{16}$$

where τ is the dimensionless time, E_{shear} is the shear strain energy, and K_{ijkl} is a kinetic coefficient characterizing the evolution of plastic deformation. E_{shear} is given by

$$E_{\mathrm{shear}} = \int_{\mathbf{r}} \left[\frac{1}{2} C_{ijkl}(\mathbf{r}) e_{ij}^{\mathrm{el}}(\mathbf{r}) e_{kl}^{\mathrm{el}}(\mathbf{r}) - s_{ij}^{\mathrm{appl}} \overline{e}_{ij} \right] d\mathbf{r}, \tag{17}$$

where e_{ij} and s_{ij} are the deviatoric strain and stress, respectively. Eq. (16) can be written as $\partial \varepsilon_{ij}^{\mathrm{p}} / \partial \tau = K_{ijkl} s_{kl}$. This equation is similar to that of the classical flow theory proposed by Reuss in which the principal axis of stress coincides with that of plastic strain increment [29]. It has been reported that dislocation activity is generally confined in the γ channels in the initial stage of high-temperature creep [1]. Hence, the shear of the γ' phase is not considered in this study. In our simulation, the von Mises yield criterion is assumed at each location in

the γ matrix, and an elastic–perfectly plastic relationship is assumed for simplicity. When the von Mises criterion is exceeded at any location in the γ phase ($\mathbf{r}_p$), the plastic strain value is determined by solving Eq. (16).

2.3. Evolution of creep strain

The creep strain ε_{kl}^c in Eq. (13) is defined as time-dependent plasticity (creep plasticity). On the basis of the von Mises-type creep theory [30], which is applicable to isotropic materials, the evolution of creep strain is given by

$$\frac{\partial \varepsilon_{ij}^c(\mathbf{r},t)}{\partial t} = \frac{3}{2} \frac{s_{ij}(\mathbf{r},t)}{\overline{\sigma}(\mathbf{r},t)} \frac{\partial \overline{\varepsilon}^c(\mathbf{r},t)}{\partial t}, \tag{18}$$

where s_{ij} is the deviatoric stress, $\overline{\sigma}$ is the equivalent stress, and $\overline{\varepsilon}^c$ is the equivalent creep strain. According to a previous report on creep in the [001]-oriented Ni−20 mass% Cr single crystal [17], the creep rate barely decreases in the early stage of transient creep, and a five-power-law behavior is observed at strains up to 0.01. In other words, in transient creep with low strains, the γ-phase alloy exhibits creep behavior similar to that observed in steady-state creep. Accordingly, at constant temperature, the creep rate can be given by the following equation similar to Norton's law:

$$\frac{\partial \varepsilon^c(\mathbf{r},t)}{\partial t} = C\sigma^5(\mathbf{r},t), \tag{19}$$

where C is a material constant. We assume that Eq. (19) is applicable to a multiaxial stress condition. By substituting Eq. (19) in Eq. (18), the evolution of creep strain is described by

the following equation:

$$\frac{\partial \varepsilon_{ij}^{c}(\mathbf{r},t)}{\partial t} = \frac{3}{2} C \overline{\sigma}^{4}(\mathbf{r},t) s_{ij}(\mathbf{r},t) .$$ (20)

Not only the plastic strain but also the creep strain is confined in the γ matrix phase; hence, Eq. (20) is solved only in the γ-phase region.

2.4. Simulation conditions

A two-dimensional (2D) phase-field simulation is performed using generalized plane strain approximation. Eqs. (2) and (3) are solved numerically by the difference method under the assumption of periodic boundary conditions. We used a 32×32 computational cell having a unit grid size of 8 nm, leading to a system size of 256×256 nm^2. The simulation parameters used in this study are listed in Table 1. The Gibbs energy coefficients are determined on the basis of the Gibbs energy calculations following the free energy model for a Ni–Al system [31]. The double-well potential height and gradient energy coefficient are fitted to the interfacial energy per area, $\gamma_{s} = 0.0142$ J m^{-2}, in the Ni–Al alloys [32]. The elastic constants and the lattice misfit of the practical alloy, CMSX-4, are employed [33,34]. A proof stress of 0.5% for the single crystal of a single-phase γ alloy [35] is used as the yield stress.

The physical parameters are converted to dimensionless quantities by using the scaling factors of RT for energy and l for length, where R is the gas constant, T is the absolute temperature, and l is the unit grid size. The time scale is transformed to dimensionless time by using $t^{*} = t \times (MRT / l^{2})$, where the asterisk denotes a dimensionless quantity. Here, M is the diffusion mobility as shown previously in Eq. (2). In Eqs. (2) and (3), the diffusion

mobility, M, and the structural relaxation coefficient, L, are set as $M^* = 2$ and $L^* = 5$, respectively, to ensure that the process of microstructure evolution is diffusion-controlled [21]. The kinetic coefficient in Eq. (16) is assumed to be $K_{ijkl} = K\delta_{ik}\delta_{jl}$, where K is $K^* = 0.002$ in dimensionless unit. The material constant, C, in Eq. (20), is set as $C^* = 0.3$; this constant is determined such that the simulation reproduces the curve of creep rate versus time of CMSX-4 at 1273 K under an external tensile stress of 160 MPa along the [001] direction. The unit time steps are selected as $\Delta t^* = 0.2$ and $\Delta\tau = 0.0002$ to maintain numerical accuracy and stability.

3. Results

3.1. Initial microstructure

The initial microstructure is prepared by the simulation based on Eqs. (2) and (3). First, we place a square γ' phase at the center of the 32×32 computational cell. The edge length of the γ' particle is 208 nm and the volume fraction of the γ' phase is 66%. Next, the simulation of microstructure evolution is performed without considering the external stress and calculation of both plastic and creep strains. This simulation relaxes the coherent strain energy and gradient energy, and smoothens both sharp edges and corners of the square γ' phase [8]. As a result, an equilibrium shape of the γ' phase is obtained, as shown in the white area of Fig. 1. In the figure, the γ phase is shown in black. As mentioned earlier, the periodic boundary conditions are assumed in this simulation; hence, the initial microstructure has the periodic array of the γ' particles aligned along <10> crystallographic directions. Furthermore, we consider only one particle and different domains in the γ' phase are not considered. In this simulation, order parameter fields, $\phi_i(\mathbf{r}, t)$ ($i = 1, 2, 3, 4$), are simply replaced by $\phi(\mathbf{r}, t)$.

3.2. Distribution of equivalent plastic strain and equivalent stress immediately after loading

Figure 2 shows the simulation results of the spatial distribution of (a) equivalent plastic strain and (b) equivalent stress, immediately after loading an external tensile stress of 160 MPa along the [01] direction. The evolution of the plastic strain is calculated by solving Eq. (16) iteratively until the equivalent stress becomes less than the yield stress in the entire γ-phase region. It is found that the plastic strain is concentrated in the γ channels that are normal to the applied stress; conversely, the stress state is almost uniform in the entire γ-phase region. Although this result is obtained from 2D analysis, it is qualitatively consistent with the analysis on dislocation channel preference by N. Zhou et al. [7], i.e., for a negative lattice misfit ($\varepsilon_0 < 0$), dislocations exist in the γ channels normal to the loading direction under external tensile stress. In addition, it is seen that the γ' phase is under a high-stress state because the shear of the γ' phase is not considered in this calculation. The macroscopic elastic and plastic strains along the external stress are calculated as 0.199% and 0.076%, respectively. The instantaneous strain is calculated as 0.275% if it is regarded as the sum of the elastic and plastic strains, whereas the experimental instantaneous strain is measured as 0.186% [36]. It is difficult to compare the absolute value of the calculated strain with the experimental result because it is hard to measure strictly the instantaneous strain in creep tests.

3.3. Creep deformation and γ' rafting

Figure 3 (a) shows the simulation result of the microstructure evolution during creep at 1273 K under a tensile stress of 160 MPa along the [01] direction. Time t^* in Fig. 3 is the dimensionless time, as mentioned in Section 2.4. The spatial distribution of equivalent inelastic strain $\bar{\varepsilon}^{\mathrm{p}} + \bar{\varepsilon}^{\mathrm{c}}$ and equivalent inelastic strain rate $\dot{\bar{\varepsilon}}^{\mathrm{p}} + \dot{\bar{\varepsilon}}^{\mathrm{c}}$ in the γ phase at the times corresponding to those of the evolving microstructure are also shown in Figs. 3 (b) and

13

(c), respectively. Here, inelastic strain is defined as the sum of the plastic and creep strains. The γ' phase begins to evolve gradually toward the direction normal to the applied stress, as shown in Fig. 3 (a) at $t^* = 6000$ s*. This microstructure evolution originates from the chemical potential difference in different types of γ channels; as reported previously, the γ-channel plasticity has a dominant role in this phenomenon [6–10]. At $t^* = 6000$ s*, internal stress is greatly relaxed not only by the creep strain introduced in the γ phase but also by the microstructure evolution of the γ' phase. Figure 3 (c) shows that at $t^* = 6000$ s*, the strain rate decreases in the entire γ-phase region compared to that at $t^* = 200$ s*. Moreover, at $t^* = 6000 - 24000$ s*, further evolution of the γ' morphology leads to the formation of the rafted structure. Fig. 3 (b) shows that the inelastic strain region gradually spreads in the γ phase as the rafting phenomenon progresses. The strain rate increases temporarily at the γ/γ' interface as shown in Fig. 3 (c) at $t^* = 14400$ s*, when the edges of the γ' phase connect with each other near the periodic boundary. After $t^* = 24000$ s*, the morphological evolution of the γ' phase does not occur in this simulation.

Figure 4 shows the spatial distribution of the creep strain rate ($\dot{\bar{\varepsilon}}^c$) and the plastic strain rate ($\dot{\bar{\varepsilon}}^p$) at $t^* = 14400$ s*. The increase in the inelastic strain rate at the rafting completion time primarily originates from the evolution of the creep strain (time-dependent inelastic strain). Hence, the equivalent stress of a large part of the γ-phase region is still less than the yield stress even at the time when the rafting phenomenon occurs.

In Fig. 5, the creep rate versus time curve obtained from the simulation is shown by solid symbols. In the initial stage of creep, the creep rate decreases monotonously by approximately $t^* = 6000$ s* as a result of the relaxation of the internal stress in the γ phase. The creep rate increases at $t^* = 14400$ s*, which corresponds to the rafting completion time. Thereafter, the creep rate continues to decrease in the simulation. For comparison, the open symbols shown in Fig. 5 denote the creep rate versus time curve of CMSX-4 at 1273 K under a tensile stress of 160 MPa along the [001] direction [2]. The time to minimum creep rate in

14

CMSX-4 is assumed to be $t = 200$ h as indicated by the arrow in Fig. 5. By fitting the rafting completion time, the time step in the simulation and real-time experiment are conformed to each other; increase in the creep rate in CMSX-4 at approximately $t = 8$ h is considered as the rafting completion time in this study. Hence, the diffusion mobility in Eq. (2) is assumed to be $M = 3.02 \times 10^{-21}$ J^{-1} mol m^2 s^{-1}. The experimental result is successfully reproduced by the simulation at the point at which the slopes of the creep rate versus time curves at the initial stage of transition creep are consistent with each other. However, the rafting completion time appears more apparent in the simulation; increase in the creep rate is evident compared to that in the experiment. The accelerating creep stage is not reproduced by the simulation and there is a large discrepancy between the simulated and experimental curves after $t = 15$ h.

4. Discussion

Figure 6 shows the evolution of the (γ + γ') microstructure obtained by 2D phase-field simulation under a tensile stress of 160 MPa along the [01] direction. Figures 6 (a) and (b) correspond to results with and without considering the inelastic strain in the γ phase (results of elasto-plastic and elastic analyses), respectively. It should be noted that rafting occurs only with inelastic strain in γ channels. Further continuation of the simulation after $t^* = 24000$ s* does not lead to any morphological evolution. According to the classical work by S. Socrate and D. M. Parks [6], the creep flow in the γ phase increases the driving force for directional coarsening by one order of magnitude greater than that obtained by elastic analysis. In addition, N. Zhou et al. calculated the chemical potential difference between the horizontal and vertical channels with respect to the loading direction and demonstrated that the γ-channel plasticity leads to a larger driving force for rafting compared to that derived strictly from the elastic modulus mismatch between the γ and γ' phases [8]. The simulation results shown in

15

Fig. 6 correspond well with these analyses, indicating that the inelastic strain in the γ phase plays a dominant role in the rafting phenomenon. However, it has been reported that the elastic analysis by a three-dimensional (3D) phase-field simulation eventually leads to the formation of a rafted structure [8], a phenomenon that is not observed in this study. This inconsistency possibly originates either from the difference in the physical parameters used in the simulation or from the difference between 2D and 3D analyses.

The creep rate versus time curve is used for comparing the result of the simulation to that of the creep of CMSX-4, as shown in Fig. 5. As mentioned in Section 3.3, the simulation time step and real time are matched by assuming that the rafting completion time (increase in the creep rate) in the experiment is approximately $t = 8$ h. Figure 7 shows the micrographs of CMSX-4: (a) before the creep test and (b) crept at 1273 K under a tensile stress of 160 MPa for 30 h. The initial microstructure exhibits an array of cubic γ' particles that precipitated coherently in the γ phase, as shown in Fig. 7 (a). The rafted structure is partially observed in the crept sample, as indicated by arrows in Fig. 7 (b). In the experiment, it is assumed that the inhomogeneous progress of the rafting phenomenon leads to the coexistence of cuboidal and rafted structures, as shown in Fig. 7 (b), and blurs the sharp increase in the creep rate, as shown in Fig. 5. However, it can be inferred that the rafting phenomenon started before $t = 30$ h, and the increase in the creep rate at approximately $t = 8$ h is due to the rafting phenomenon. In specific alloy systems, it is often reported that the "S-shaped" creep strain versus time curve is clearly observed in the primary stage of creep at high temperatures under low stresses [37]. The simulation results in this paper demonstrate that the "S-shaped" creep curve is related to the formation of the rafted structure.

In our simulation, the creep rate continues to decrease, as shown in Fig. 5, and the accelerating creep is not reproduced. Figure 8 shows the spatial distribution of equivalent stress obtained from the simulation: (a) $t^* = 24000$ s* and (b) $t^* = 180000$ s*. The equivalent stress in the γ phase decreases with time; this is due to the time evolution of the

creep strain in the γ phase. The change in the equivalent stress directly affects the creep strain increment, which is calculated from Eq. (20), and hence, the creep rate keeps decreasing in the simulation except at the rafting completion time. In the simulation, the microstructure evolution does not occur after the formation of the rafted structure with ideal lamellas. However, it has been reported that the rafted structure collapses in the latter creep stage; the γ-channel thickness increases [2] or the lamellar structure develops waves [3–5]. These phenomena can be attributed to the loss of interfacial coherency, the coalescence of the γ' phase, and/or change in the morphological stability of the rafted structure during creep [5,11,12]. If such microstructure evolution is reproduced in a large-scale simulation that involves many precipitates and microstructural inhomogeneity (spatial variation of the γ/γ' microstructure), the stress state in the γ phase would be changed, and the increase in the creep rate could be reproduced. The creep rate in the accelerating creep stage is closely related to the increase in the γ/γ' lamellar thickness, namely, microstructure evolution [2].

In the phase-field model of dislocations, the sheared region enclosed by a dislocation loop is described as a plate with thickness equal to the interplanar spacing [38]. The eigenstrain of the plate is given by $\varepsilon_0 = (\mathbf{n} \otimes \mathbf{b} + \mathbf{b} \otimes \mathbf{n})/2d$, where d is the interplanar spacing, $\mathbf{n}$ is the unit vector of the slip plane, and $\mathbf{b}$ is Burgers vector. In a simulation study on Ni−Al single crystal [39], this description has been extended by introducing a new set of local dislocation density fields for characterizing the γ-channel plastic deformation on the micrometer scale. It is expected that this model will lead to the quantitative reproduction of creep deformation by rigorous treatment of the mobility of plastic strain fields [39]. The macroscopic strain evolution model is adopted to describe the γ-channel plasticity in this study. The advantage of our model is that the macroscopic experimental data on γ-phase mechanical properties can be incorporated in strain evolution equations. In this study, by referring to the tensile and creep properties previously reported for single-crystal γ alloys and fitting the simulation results to the experimental data, the creep rate versus time curve is

successfully reproduced in the initial stage of the transition creep in CMSX-4.

A limitation of this model is caused by Eq. (20), which is valid only for strain levels up to 0.01. Furthermore, for improved quantitative simulations, a rigorous model that incorporates the anisotropic mechanical properties of single-crystal γ alloys [15−17] may be necessary. Our model lacks anisotropic calculations of the inelastic strain evolution, as shown in Eqs. (16) and (20). In future studies, 3D analysis may also be necessary. For the same volume fraction of the γ' phase, the γ-channel widths in 2D and 3D analyses differ from each other. This difference seems to cause the discrepancy in the diffusion mobility M, namely, rafting kinetics. It is expected that a large-scale simulation using our model and having the physical parameters of multi-component practical alloys as its input would reproduce the creep rate versus time curve of nickel-based superalloys at high temperatures under low-stress conditions.

5. Conclusions

A phase-field model is developed by considering the evolution of both $(\gamma + \gamma')$ microstructure and inelastic strain in the γ phase during creep in nickel-based superalloys. Inelastic strain is defined as the sum of two components: time-independent inelastic strain and time-dependent inelastic strain. To describe the inelastic strain evolution, the classical flow and creep theories are adopted in which experimentally reported mechanical properties of γ-phase alloys are incorporated.

The 2D phase-field simulation reproduces the dislocation channel preference immediately after loading the external tensile stress; the inelastic strain is concentrated in the γ channels normal to the loading direction. By fitting creep response from the simulation to the experimental data, the creep rate versus time curve of CMSX-4 is successfully reproduced; the slopes of the experimental and simulated curves in the initial stage of

transition creep are consistent well with each other. The rafting phenomenon during creep is also reproduced. At rafting completion time, increase in the creep rate is observed in the simulation, whereas it is obscured in CMSX-4. It is demonstrated that the creep rate increases at γ/γ' interfaces when the rafted structure is formed.

Acknowledgements

References

[1] Pollock TM, Argon AS. Acta Metall Mater 1994;42:1859.

[2] Miura N, Kondo Y, Matsuo T. Tetsu to Hagane 2003;89:1240.

[3] Murata Y, Hashizume R, Yoshinari A, Aoki N, Morinaga M, Fukui Y. Superalloys 2000. Warrendale, PA: The Minerals, Metals & Materials Society; 2000. p. 285.

[4] Epishin A, Link T, Portella PD, Brückner U. Acta Mater 2000;48:4169.

[5] Tanaka K, Ichitsubo T, Kishida K, Inui H, Matsubara E. Acta Mater 2008;56:3786.

[6] Socrate S, Parks DM. Acta Metall Mater 1993;41:2185.

[7] Zhou N, Shen C, Mills MJ, Wang Y. Acta Mater 2007;55:5369.

[8] Zhou N, Shen C, Mills MJ, Wang Y. Acta Mater 2008;56:6156.

[9] Zhou N, Shen C, Sarosi PM, Mills MJ, Pollock T, Wang Y. Mater Sci Technol 2009;25:205.

[10] Gaubert A, Le Bouar Y, Finel A. Philos Mag 2010;90:375.

[11] Tsukada Y, Murata Y, Koyama T, Morinaga M. Mater Trans 2008;49:484.

[12] Tsukada Y, Murata Y, Koyama T, Morinaga M. Proceedings of the 9th Liège Conference on Materials for Advanced Power Engineering; 2010. p. 751.

[13] Li DY, Chen LQ. Scr Mater 1997;37:1271.

[14] Tsukada Y, Murata Y, Koyama T, Morinaga M. Mater Trans 2009;50:744.

[15] Siebörger D, Glatzel U. Acta Mater 1999;47:397.

[16] Terada Y, Yasui T, Matsuo T. Mater Sci Forum 2003;426–432:785.

[17] Tokumoto T, Terada Y, Matsuo T. Mater Sci Forum 2003;426–432:803.

[18] Guo XH, Shi SQ, Ma XQ. Appl Phys Lett 2005;87:221910.

[19] Guo XH, Shi SQ, Zhang QM, Ma XQ. J Nucl Mater 2008;378:110.

[20] Guo XH, Shi SQ, Zhang QM, Ma XQ. J Nucl Mater 2008;378:120.

[21] Zhu JZ, Wang T, Ardell AJ, Zhou SH, Liu ZK, Chen LQ. Acta Mater 2004;52:2837.

[22] Chen LQ. Annu Rev Mater Res 2002;32:113.

[23] Zhu JZ, Wang T, Zhou SH, Liu ZK, Chen LQ. Acta Mater 2004;52:833.

[24] Cahn JW, Hilliard JE. J Chem Phys 1958;28:258.

[25] Kim SG, Kim WT, Suzuki T. Phys Rev E 1999;60:7186.

[26] Khachaturyan AG. Theory of Structural Transformations in Solids. New York: Dover; 2008.

[27] Mura T. Micromechanics of Defects in Solids, second revised ed. Dordrecht: Kluwer Academic; 1987.

[28] Hu SY, Chen LQ. Acta Mater 2001;49:1879.

[29] Hill R. The Mathematical Theory of Plasticity. Oxford: Oxford University Press; 1998.

[30] Odqvist Folke KG. Mathematical Theory of Creep and Creep Rupture. London: Oxford University Press; 1966.

[31] Ansara I, Dupin N, Lukas HL, Sundman B. J Alloys Compd 1997;247:20.

[32] Ardell AJ. Acta Metall 1968;16:511.

[33] Siebörger D, Knake H, Glatzel U. Mater Sci Eng A 2001;298:26.

[34] Glatzel U. Scr Metall Mater 1994;31:291.

[35] Yeh AC, Tin S. Scr Mater 2005;52:519.

[36] Miura N, Kondo Y. Unpublished result.

[37] Izuno H, Yokokawa T, Koizumi Y, Odaka S, Harada H. J Japan Inst Metals 2004;68:526.

[38] Wang YU, Jin YM, Cuitiño AM, Khachaturyan AG. Acta Mater 2001;49:1847.

[39] Zhou N, Shen C, Mills M, Wang Y. Philos Mag 2010;90:405.

Captions:

Table 1 Simulation parameters used in this study

Fig. 1 Initial microstructure before creep, prepared using phase-field simulation. Black and white areas correspond to the γ and γ' phases, respectively.

Fig. 2 Simulation results of the spatial distribution of (a) equivalent plastic strain ($\bar{\varepsilon}^{\mathrm{p}}$) and (b) equivalent stress ($\bar{\sigma}$), immediately after loading a tensile stress of 160 MPa along the [01] direction.

Fig. 3 Results of 2D phase-field simulation during creep at 1273 K under a tensile stress of 160 MPa along the [01] direction: (a) (γ + γ') microstructure evolution with creep time, (b) time evolution of the spatial distribution of equivalent inelastic strain, and (c) time evolution of the spatial distribution of equivalent inelastic strain rate. Inelastic strain is defined as the sum of plastic strain (ε^{p}) and creep strain (ε^{c}). Time t^{*} is the dimensionless time.

Fig. 4 Simulation results of the spatial distribution of equivalent inelastic strain rate at $t^{*} = 14400$ s*, when the rafted structure is formed: (a) equivalent creep strain rate ($\dot{\bar{\varepsilon}}^{\mathrm{c}}$) and (b) equivalent plastic strain rate ($\dot{\bar{\varepsilon}}^{\mathrm{p}}$). Time t^{*} is the dimensionless time.

Fig. 5 Creep rate versus time curves obtained from the 2D phase-field simulation (solid symbols) and from the creep on CMSX-4 (open symbols) at 1273 K under a tensile stress of 160 MPa along the [001] direction [2]. The arrow indicates the time to minimum creep rate in CMSX-4.

Fig. 6 Evolution of (γ + γ') microstructure obtained by 2D phase-field simulation at 1273 K under a tensile stress of 160 MPa along the [01] direction: (a) considering inelastic strain in the γ phase and (b) without considering inelastic strain in the γ phase. Black and white areas correspond to the γ and γ' phases, respectively. Time t^* is the dimensionless time.

Fig. 7 Micrographs of CMSX-4: (a) before creep test and (b) crept at 1273 K under a tensile stress of 160 MPa for 30 h. White arrows indicate the rafted structure that was partially formed during creep.

Fig. 8 Simulation results of the spatial distribution of equivalent stress: (a) $t^* = 24000$ s* and (b) $t^* = 180000$ s*. Time t^* is the dimensionless time.

Temperature, T / K	1273
Gibbs energy coefficients, W / J m^{-3}	$W_m = 2.58 \times 10^8$, $W_p = 3.11 \times 10^8$
Double-well potential height, w / J m^{-3}	1.07×10^7
Gradient energy coefficient, κ_ϕ / J m^{-1}	3.41×10^{-10}
Volume fraction of the γ' phase	66%
Elastic constants, C_{ijkl} / GPa	$C^m_{11} = 204.9$, $C^m_{12} = 150.8$, $C^m_{44} = 94.0$ $C^p_{11} = 251.6$, $C^p_{12} = 194.5$, $C^p_{44} = 95.0$
Lattice misfit, ε_0	-0.0023
External stress along the [01] direction, σ^{appl} / MPa	160
Yield stress of the γ phase, σ_y / MPa	120

Figure 1
Click here to download high resolution image
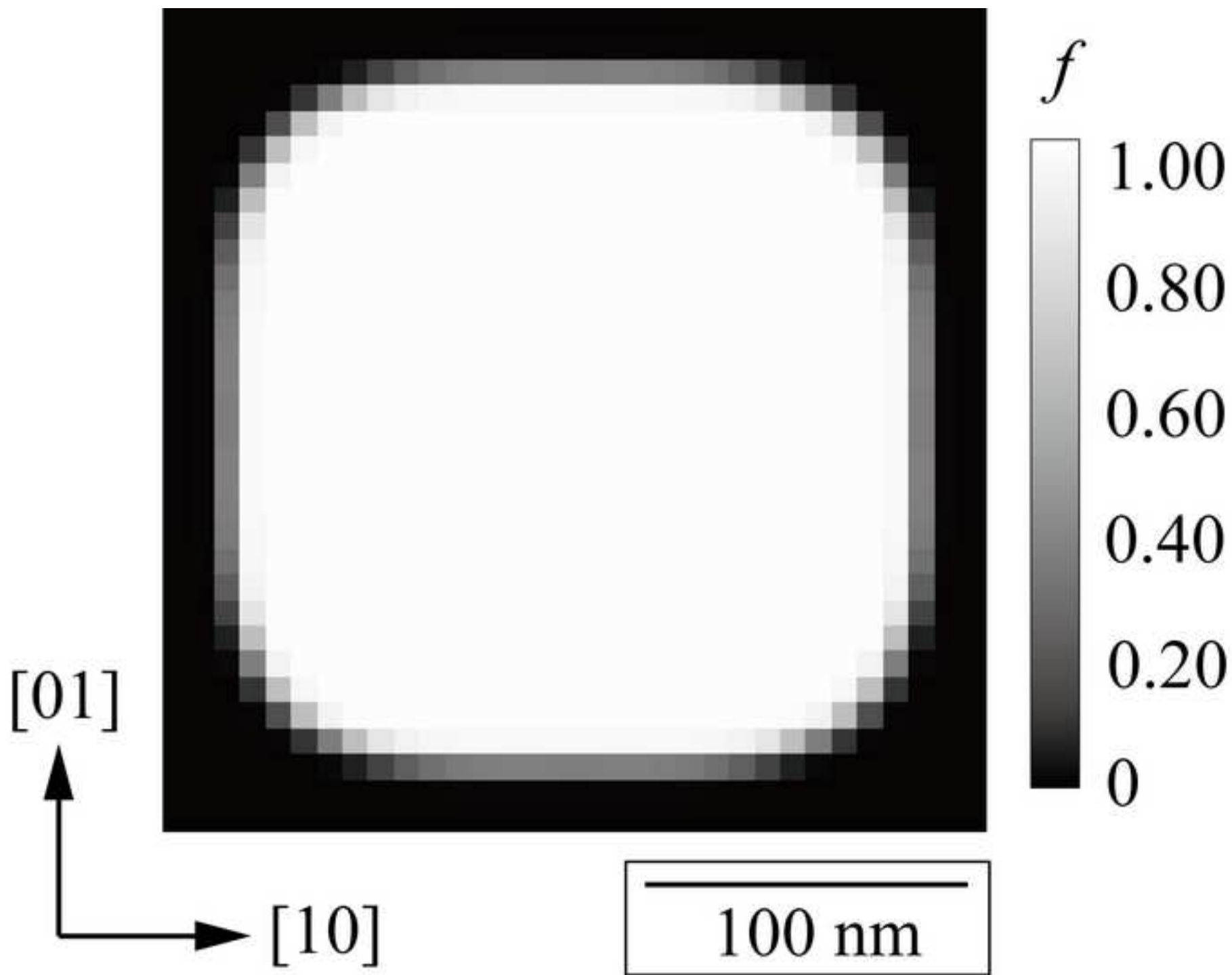
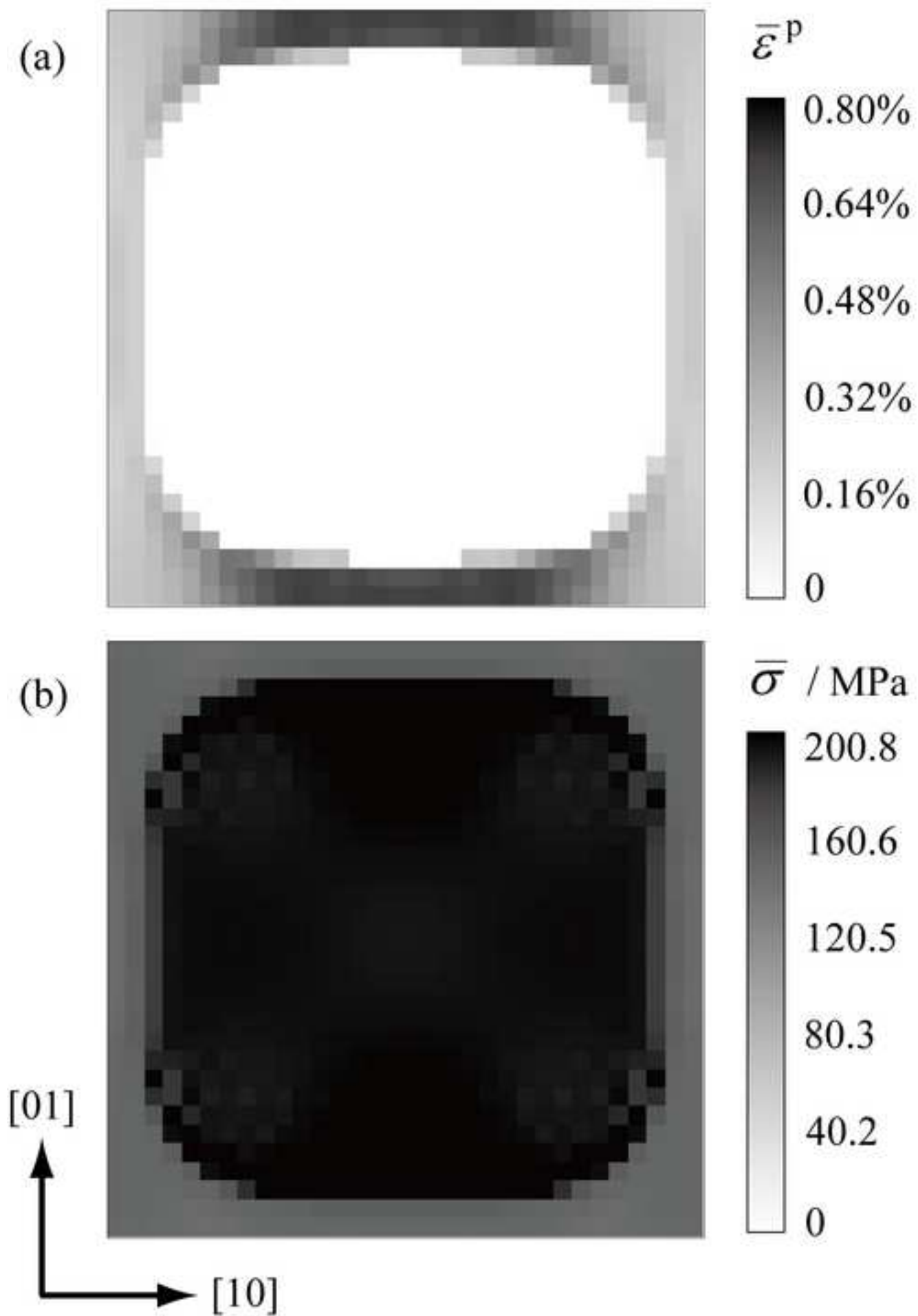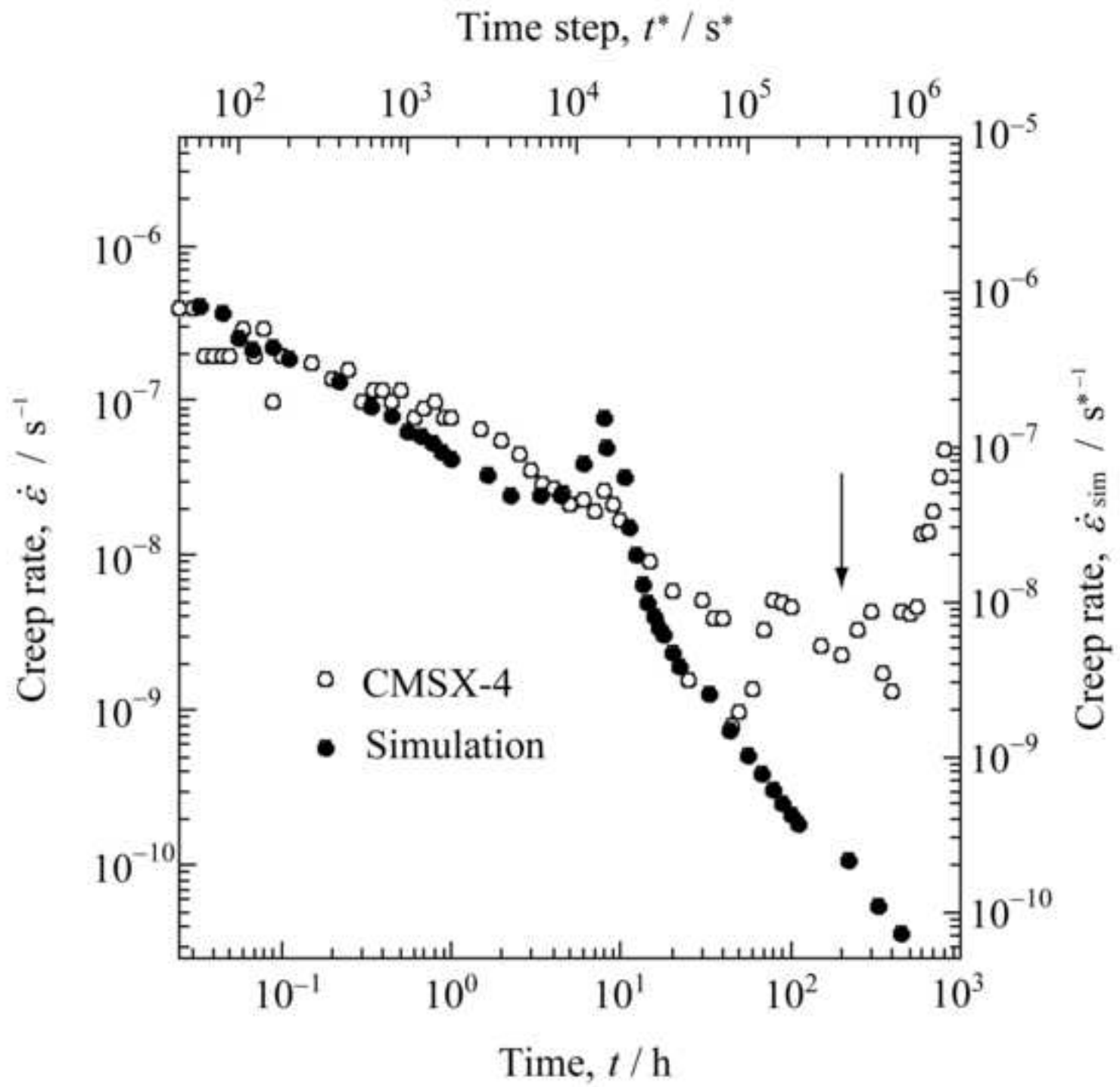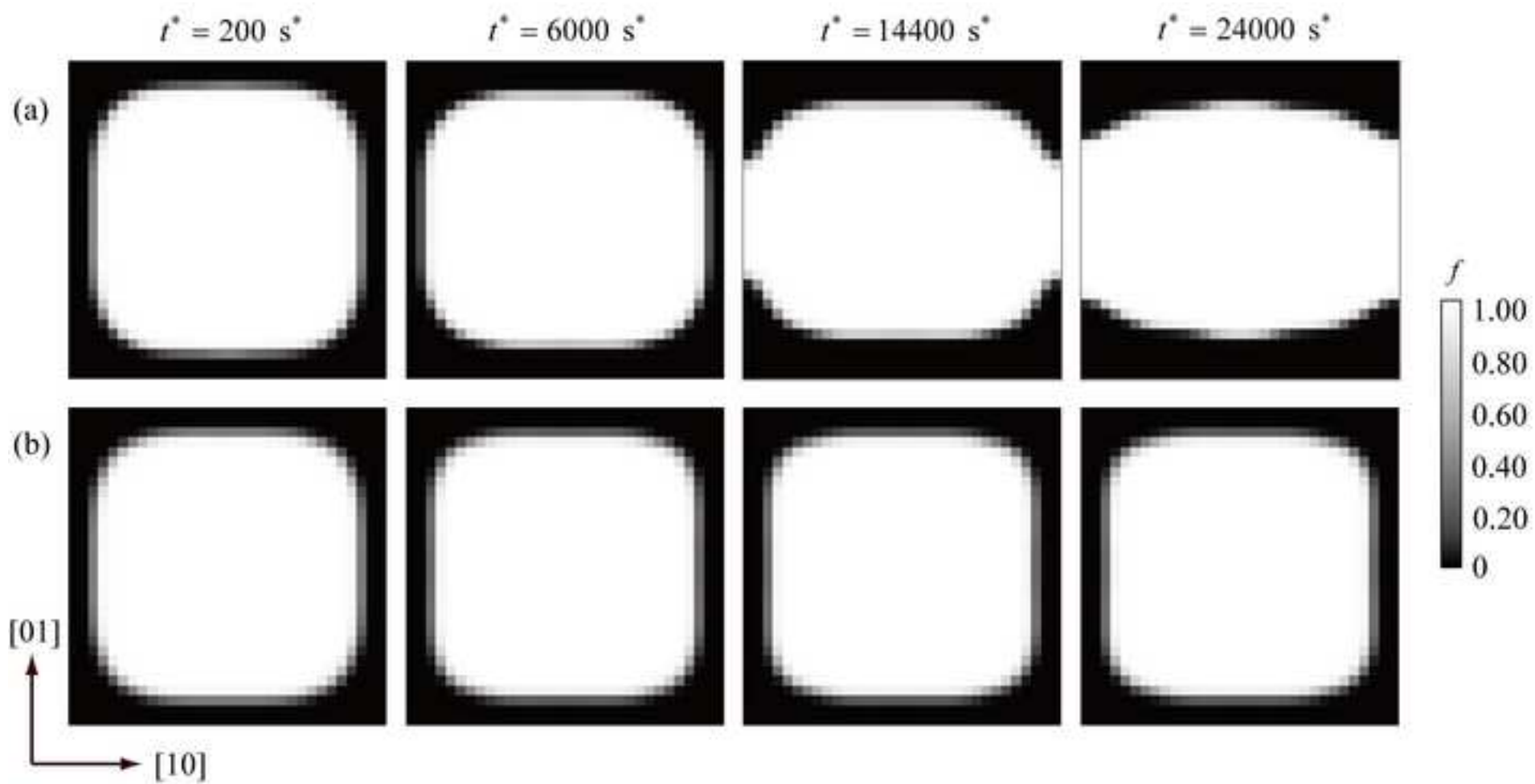**Figure 2**
Click here to download high resolution image

(a)

$\bar{\varepsilon}^{\mathrm{p}}$

0.80%

0.64%

0.48%

0.32%

0.16%

0

(b)

$\bar{\sigma}$ / MPa

200.8

160.6

120.5

80.3

40.2

0

[01]

[10]

Figure 3
Click here to download high resolution image
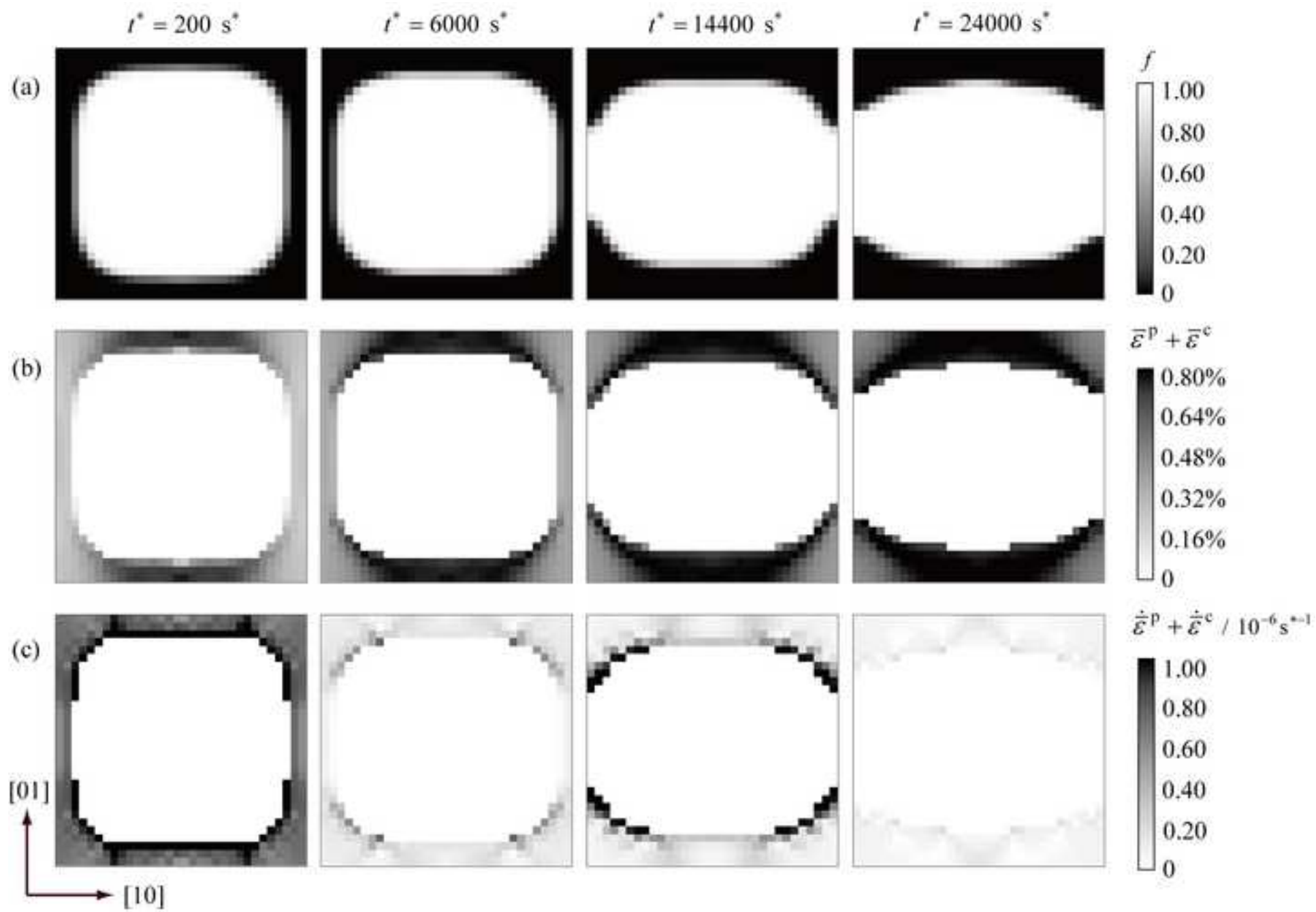
Figure 3

Figure 4
Click here to download high resolution image

(a)

$\dot{\bar{\varepsilon}}^{c}$ / 10^{-6} s^{*-1}

1.00

0.80

0.60

0.40

0.20

0

(b)

$\dot{\bar{\varepsilon}}^{p}$ / 10^{-6} s^{*-1}

1.00

0.80

0.60

0.40

0.20

0

[01]

[10]
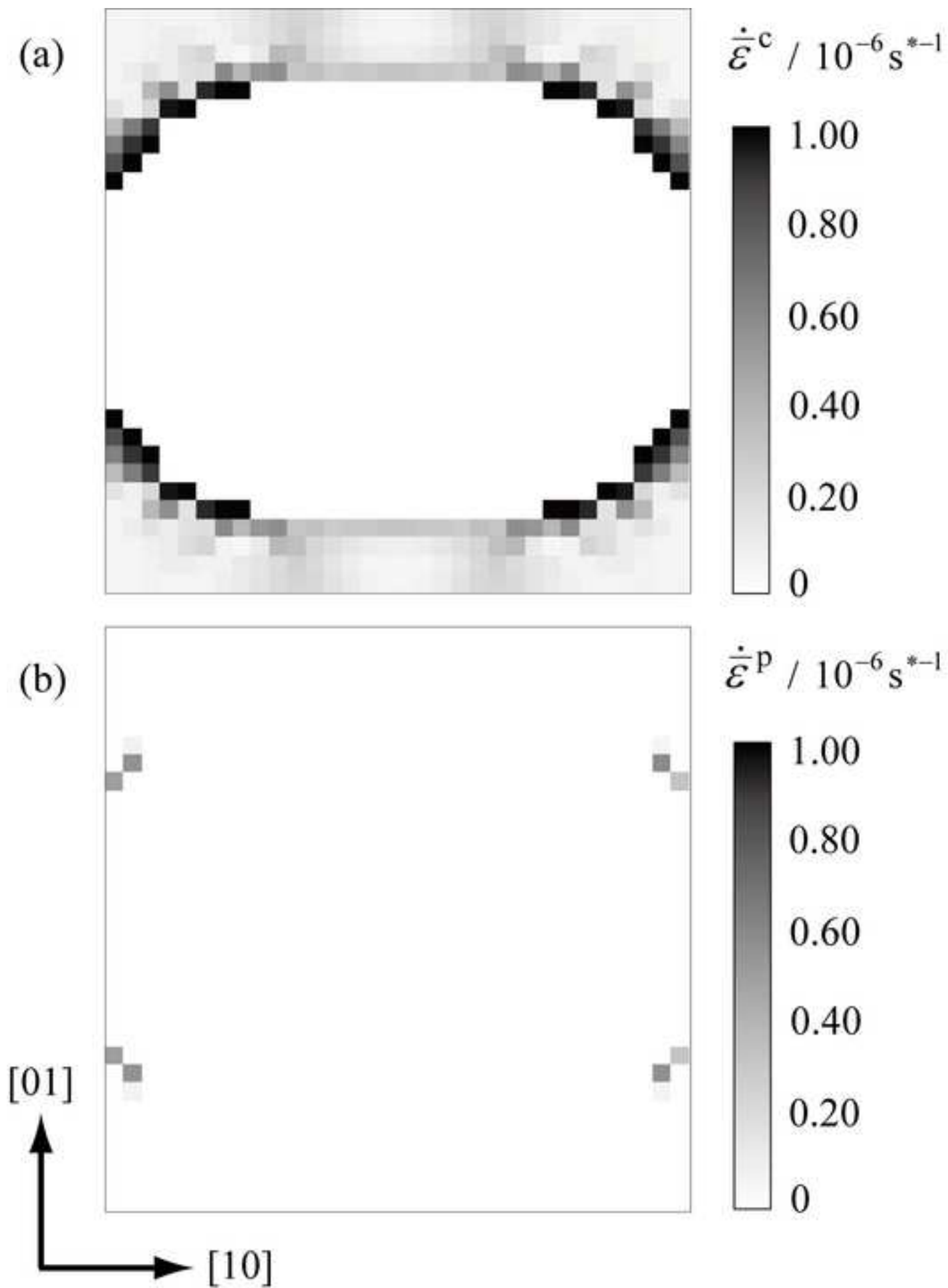
Figure 5
Click here to download high resolution image

Figure 5

Figure 6
Click here to download high resolution image

$t^* = 200 \ s^*$ $t^* = 6000 \ s^*$ $t^* = 14400 \ s^*$ $t^* = 24000 \ s^*$

(a)

(b)

f

1.00

0.80

0.60

0.40

0.20

0

[01]

[10]

Figure 7
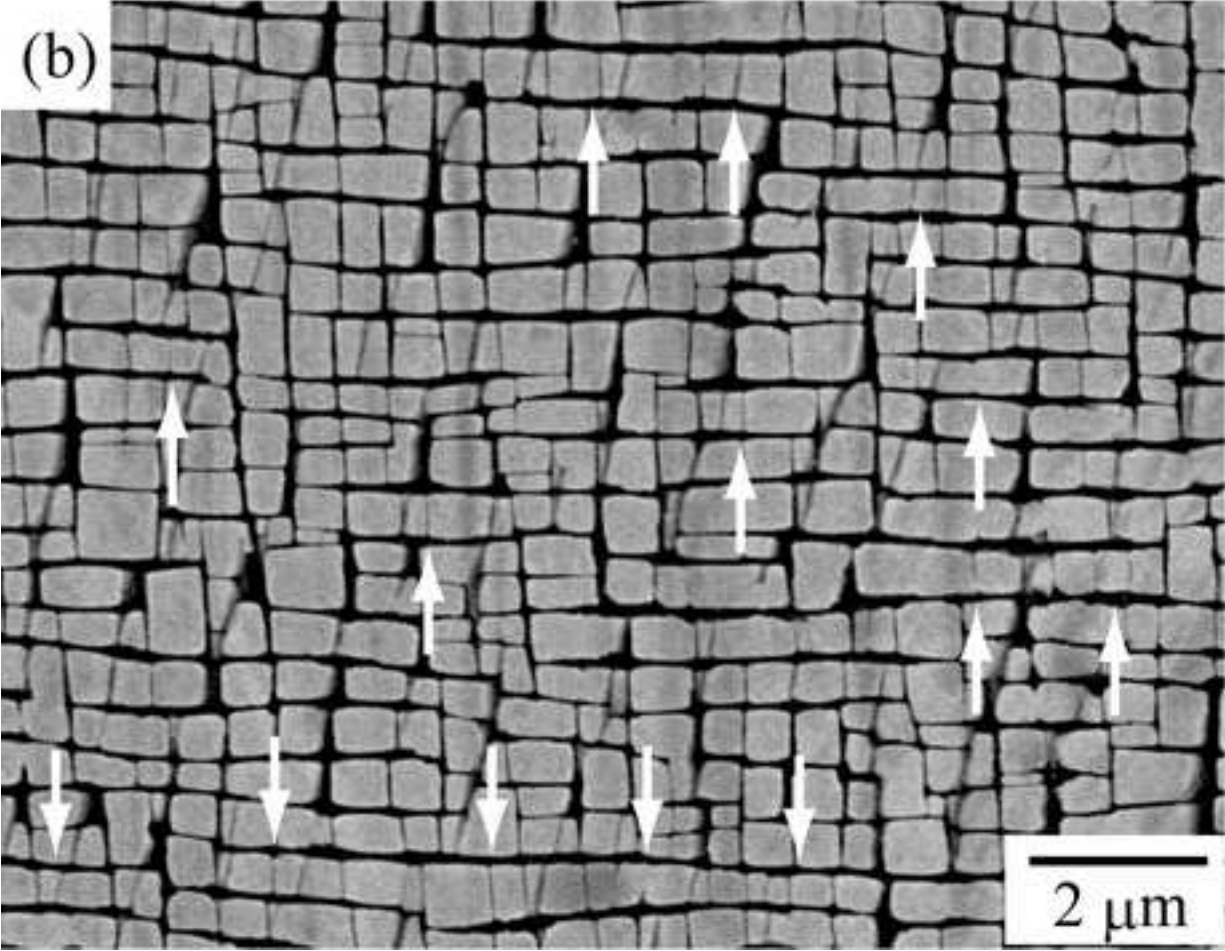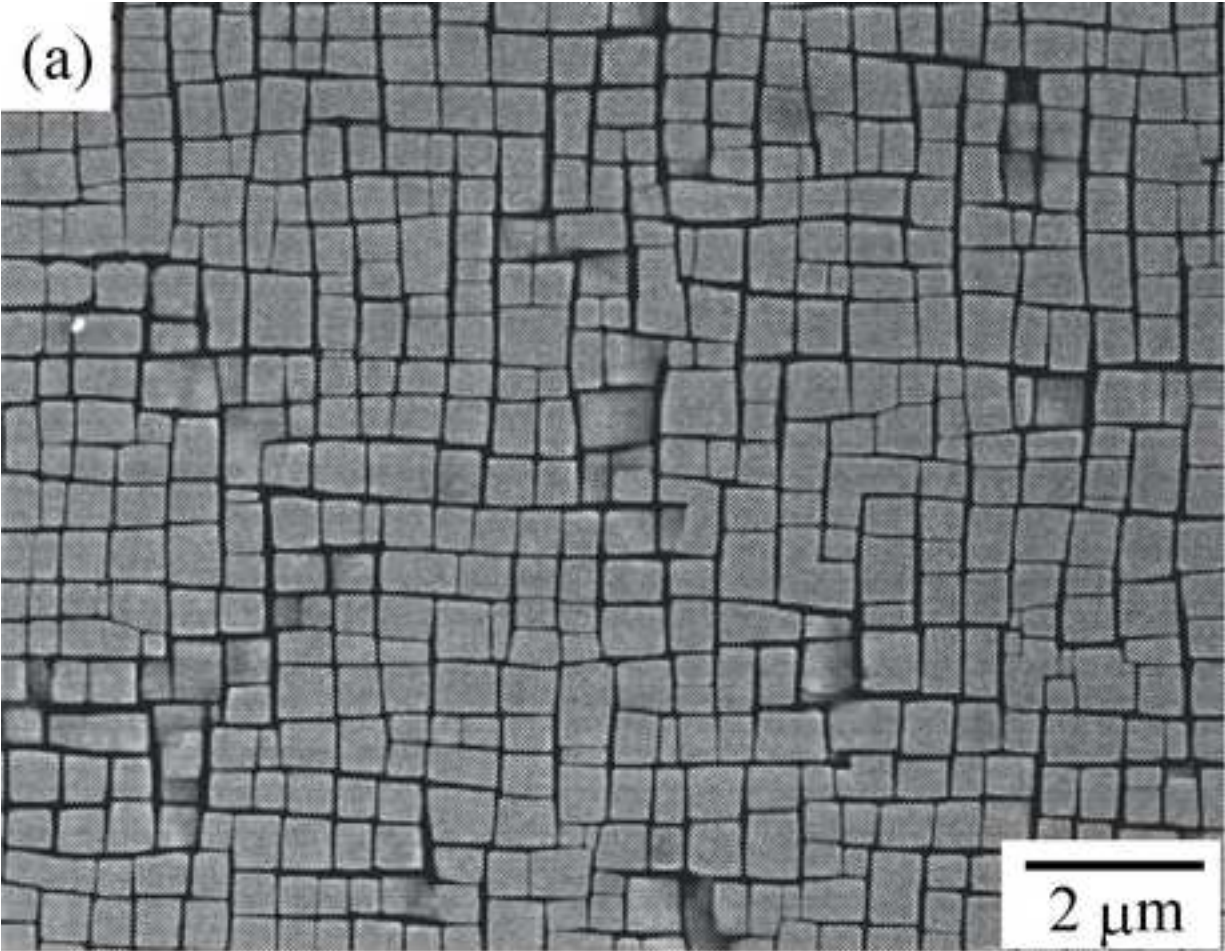Click here to download high resolution image

(a)

2 μm

(b)

2 μm

Figure 8
Click here to download high resolution image